Supporting Information

Unravelling the water oxidation mechanism on NaTaO₃–based photocatalyst

Qian Ding[†,‡,⊥], Yang Liu[†,‡,⊥], Tao Chen[†,§], Xiaoyu Wang[∥], Zhaochi Feng[†], Xiuli Wang[*,†], Michel Dupuis[*,∥], Can Li[†]

[†]State Key Laboratory of Catalysis, Dalian Institute of Chemical Physics, Chinese Academy of Sciences, Dalian National Laboratory for Clean Energy, Dalian 116023, China. E-mail: xiuliwang@dicp.ac.cn

[‡]University of Chinese Academy of Sciences, Beijing 100049, China

[§] School of Marine Science and Environment Engineering, Dalian Ocean University, 52 Heishijiao Street, Dalian, 116023, China

[∥] Department of Chemical and Biological Engineering, University at Buffalo, State University of New York, Buffalo 14260, USA. E-mail: mdupuis2@buffalo.edu

[⊥] These two authors equally contributed to the work.

Table S1. Surface energies of low-index surfaces.

The surface energy is calculated by $\sigma = (E_{slab} - E_{bulk})/2S = (E_{slab} - N_{unit} \times E_{unit})/(2a \times b \times \sin\gamma)$, E_{slab} is the DFT energy of the optimized 4-layer slab, $E_{bulk} = N_{unit} \times E_{unit}$ is the energy for the same unit of $NaTaO_3$ in bulk phase (N_{unit} is the number of $NaTaO_3$ unit in the slab, $E_{unit} = -39.79$ eV is the energy of per $NaTaO_3$ unit in bulk), $S = a \times b \times \sin\gamma$ is the surface area of single side of the slab (a, b, and γ are the crystallographic parameters of the 4-layer slab). Slab for each surface was built up by direct bulk cleavage of the optimized unit cell and then introducing a 16 Å vacuum between the slabs. All the atoms in the slabs were full relaxed during the calculations.

Surface	E_{slab} /eV	N_{unit}	a /Å	b /Å	$\gamma/°$	σ /eV·Å^{-2}
(001)	-629.43	16	10.94	5.55	90.00	0.0593
(110)	-629.36	16	7.80	7.79	90.00	0.0599
($1\bar{1}0$)	-629.36	16	7.79	7.80	90.00	0.0599
(100)	-611.57	16	11.09	7.80	90.00	0.1449
(010)	-611.20	16	7.80	10.94	90.00	0.1491
(112)	-611.42	16	7.79	11.02	90.55	0.1489
($1\bar{1}2$)	-611.42	16	11.02	7.79	90.55	0.1489
(111)	-615.80	16	15.58	9.53	66.22	0.0767
($1\bar{1}1$)	-615.77	16	9.53	15.58	66.22	0.0768

Table S2. Relative DFT energetics of water oxidation intermediates to their corresponding clean surface models

For each model, $E_{relative}$(intermediate) = E_{DFT}(intermediate) - E_{DFT}(*).

Possible intermediates	Energetics /eV		
	5-2 model	4-2 model	4-1 model
* (clean surface)	0.0000	0.0000	0.0000
*OH	-12.6575	-12.6958	-11.4615
*O_s	-4.3688	-4.4209	-4.2862
*O_d	-9.4475	-9.4468	-6.3208
*OOH_s	-16.9197	-16.9511	-15.7031
*OOH_d	-16.6976	-16.766	-15.5025

The intermediates in traditional four-step proton-coupled-electron transfer (PCET) mechanism (H_2O → *OH → *O → *OOH → *OH + O_2) are optimized and their relative energies to their corresponding clean surface models were calculated (Table S2). 5-2 model, 4-2 model and 4-1 model are $NaTaO_3$ (001) slab with (five layers - two frozen layers), (four layers - two frozen layers), and (four layers - one frozen layer), respectively (shown in Figure S3). As shown in Table S2, the relative energy of *OH with the 4-1 model is ~ 1.2 eV off from the 4-2 and 5-2 models. The relative energies of *O_s are similar for all three models, while for *O_d the 4-1 relative energy is off by ~ 3.1 eV. For *OOH_s and *OOH_d the differences between models are ~ 1.2 eV. *O_d and *OOH_s are the thermodynamically favored form for *O and *OOH, respectively, giving rise to the water oxidation energy diagrams displayed in Figure S4.

Table S3. Zero-point energy corrections and entropic contributions to free energies calculated by Nørskov *et al.*[1]

	H_2O	H_2	*OH	*O	*OOH	*H_2O
ΔZPE/eV	0.56	0.27	0.35	0.05	0.41	0.70
TΔS /eV	0.67	0.41	0	0	0	0

Table S4. Photocatalytic activities of $NaTaO_3$-based photocatalysts for water splitting. 0.2 g catalyst, 500 mL H_2O, 450 W Hg lamp, online GC analysis.

Sample	H_2 evolution mmol h^{-1} g^{-1}	O_2 evolution mmol h^{-1} g^{-1}
$NaTaO_3$	0.308	0.166
$NaTaO_3$:La	0.448	0.196
$NiO/NaTaO_3$	4.453	1.767
$NiO/NaTaO_3$:La	11.965	5.987

Photocatalytic water splitting reaction was performed in a closed gas circulation system. The photocatalyst powder (0.2 g) was dispersed in well-outgassed water (500 mL) by a magnetic stirrer in an inner irradiation cell made of quartz. The light source was a 450 W high-pressure mercury lamp (USHIO UM452). The reaction temperature was maintained at 287 ± 1K. The amounts of evolved H_2 and O_2 were determined by online gas chromatography (Shimadzu; GC-8A).

To study the water oxidation mechanism experimentally, $NaTaO_3$-based photocatalysts were prepared and the photocatalytic overall water splitting activities were evaluated with UV light irradiation. For all the tests, H_2 and O_2 simultaneously evolved with the H_2/O_2 molar ratio close to 2:1. Coincident with the published results, La doping and NiO loading drastically improve the photocatalytic activity.[2]

Table S5. Photocatalytic activities of NiO/NaTaO$_3$:La for water vapor splitting. 0.05 g catalyst, 266 nm laser (20 Hz, 70 mW) irradiation, online GC analysis.

Saturated water vapor pressure / 10^3 Pa	H$_2$ evolution umol h^{-1} g^{-1}	O$_2$ evolution umol h^{-1} g^{-1}
2.4877	2.5	4.5
5.9453	3.8	3.5

The photocatalytic water vapor splitting reaction was performed in an IR cell. The photocatalyst (0.05g) was pressed into a self-supporting wafer, then water vapor was introduced into the IR cell after evacuation. The light source was a 266 nm laser (Quanta-Ray INDI Nd:YAG Laser) with pulse duration of 6-8 ns (20 Hz, 70 mW). The amounts of evolved H$_2$ and O$_2$ were determined by online gas chromatography (Agilent; GC-7890A).

The activity of the NiO/NaTaO$_3$:La photocatalyst for photocatalytic splitting of water vapor were also evaluated. The H$_2$/O$_2$ molar ratios evolved in water vapor are much smaller than the ratios of 2 in liquid water. The small H$_2$/O$_2$ molar ratio is mainly due to the low photocatalytic activity under the measurement conditions in gas phase. At the low photocatalytic activity, the adsorption problem of gas on the reactor makes the measured ratios not accurate, since the adsorption of evolved H$_2$ and O$_2$ on a large *in-situ* cell in our experiment is very serious. With a special microreactor, Dionigi et al. reported that the H$_2$/O$_2$ molar ratios of the overall water splitting photocatalyst, Rh$_{2-y}$Cr$_y$O$_3$/GaN:ZnO, in gas phase by dosing water vapor remains as

2.[3, 4] It is demonstrated that the water splitting mechanism in vapor water is the same as in liquid water. Although the activities for gas-phase photocatalytic water splitting are rather low, these results demonstrate the possibility to investigate the water oxidation mechanism under water vapor using *in situ* FTIR transmission spectroscopy.

Table S6. Energetics of possible water oxidation intermediates

Possible intermediates	Energetics /eV	
	(001) surface	(110) surface
* (clean surface)	-1566.2263	-1566.1928
*OH	-1578.8838	-1578.7409
*O_s	-1570.5951	-1570.5477
*O_d	-1575.6738	-1575.5169
*OOH_s	-1583.1460	-1583.0783
*OOH_d	-1582.9239	-1582.7993
*H_2O	-1581.1567	-1581.0352
*OH +*OH	-1591.6470	-1591.4911
*O_d +*OH	-1587.5290	-1587.3270
*OOH_s +*OH	-1595.7927	-1595.7387
*OOH_d +*OH	-1595.5418	-1595.3832
*H_2O +*OH	-1594.2910	-1594.2076
H_2O	-14.22812	
H_2	-6.769222	

Table S7. Water oxidation paths in Figure 5 and their free energy changes at pH = 7.

The free energy changes are calculated using the equations we described in

Section 3. Computational Method. Take step 3b for example,

$$\Delta G_{(001)} = \Delta E + \Delta ZPE - T\Delta S + \Delta G_{pH} = \Delta E(*OH \rightarrow *O_d + 1/2\ H_2) + \Delta ZPE(*OH$$

$$\rightarrow *O_d + 1/2\ H_2) - T\Delta S(*OH \rightarrow *O_d + 1/2\ H_2) + (-\ln 10) \times kT \times pH = [(-1575.6738)$$

$$+ 0.5 \times (-6.769222) - (-1578.8838)] + (0.05 + 0.5 \times 0.27 - 0.35) - (0 + 0.5 \times 0.41 - 0)$$

$$+ (-2.303) \times 0.0256925793 \times 7 = -0.96\ eV$$

Step	Elementary steps	$\Delta G_{(001)}$ /eV	$\Delta G_{(110)}$ /eV
1	(a) $* + H_2O \rightarrow *H_2O$	0.11	0.20
2	(a) $*H_2O \rightarrow *OH + (H^+ + e^-)$	-1.94	-1.92
	(b) $*H_2O + H_2O \rightarrow *H_2O + *OH + (H^+ + e^-)$	-2.31	-2.35
3	(a) $*OH \rightarrow *O_s + (H^+ + e^-)$	4.12	4.03
	(b) $*OH \rightarrow *O_d + (H^+ + e^-)$	-0.96	-0.94
	(c) $*OH + H_2O \rightarrow *OH + *OH + (H^+ + e^-)$	-1.93	-1.92
	(d) $*H_2O + *OH \rightarrow *OH + *OH + (H^+ + e^-)$	-1.56	-1.49
4	(a) $*O_s + H_2O \rightarrow *OOH_d + (H^+ + e^-)$	-1.51	-1.44
	(b) $*O_s + H_2O \rightarrow *OOH_s + (H^+ + e^-)$	-1.73	-1.72
	(c) $*O_d + H_2O \rightarrow *OOH_d + (H^+ + e^-)$	3.57	3.53
	(d) $*O_d + H_2O \rightarrow *OOH_s + (H^+ + e^-)$	3.35	3.25
	(e) $*O_d + H_2O \rightarrow *O_d + *OH + (H^+ + e^-)$	-1.02	-0.98
	(f) $*OH + *OH \rightarrow *O_d + *OH + (H^+ + e^-)$	-0.05	0.00
5	(a) $*OOH_d \rightarrow * + O_2 + (H^+ + e^-)$	4.14	4.05

	(b) $*OOH_d + H_2O \rightarrow *OH + O_2 + 2\ (H^+ + e^-)$	2.31	2.33
	(c) $*OOH_d + H_2O \rightarrow *OOH_d + *OH + H^+ + e^-$	-1.79	-1.75
	(d) $*OOH_s \rightarrow * + O_2 + (H^+ + e^-)$	4.36	4.33
	(e) $*OOH_s + H_2O \rightarrow *OH + O_2 + 2\ (H^+ + e^-)$	2.53	2.61
	(f) $*OOH_s + H_2O \rightarrow *OOH_s + *OH + H^+ + e^-$	-1.83	-1.84
	(g) $*O_d + *OH + H_2O \rightarrow *OOH_d + *OH + H^+ + e^-$	2.80	2.76
	(h) $*O_d + *OH + H_2O \rightarrow *OOH_s + *OH + H^+ + e^-$	2.54	2.39
	(a) $* + H_2O \rightarrow *H_2O$	0.11	0.20
6	(b) $*OOH_d + *OH + H_2O \rightarrow *OH + *OH + O_2 + 2\ (H^+ + e^-)$	2.17	2.16
	(c) $*OOH_s + *OH + H_2O \rightarrow *OH + *OH + O_2 + 2\ (H^+ + e^-)$	2.43	2.53
7	(a) $*H_2O \rightarrow *OH + (H^+ + e^-)$	-1.94	-1.92
	(b) $*OH + *OH + H^+ + e^- \rightarrow *OH + H_2O$	1.93	1.92

Table S8. The adsorption energies of intermediates on $NaTaO_3$

The adsorption energies are calculated using the equations described by Rossmeisl et al.[5] Different from the free energy change ΔG we calculated in Table S8, the adsorption energies are independent of the H^+ concentration (pH value).

$\Delta E_{*OH} = \Delta E(*OH) - \Delta E(*) - [E(H_2O) - 1/2\ E(H_2)]$

$\Delta E_{*O} = \Delta E(*O) - \Delta E(*) - [E(H_2O) - E(H_2)]$

$\Delta E_{*OOH} = \Delta E(*OOH) - \Delta E(*) - [E(H_2O) - 3/2\ E(H_2)]$

	$NaTaO_3$ (001)	$NaTaO_3$ (110)	$LaTiO_3$[5]
E_{*OH}/ eV	-1.81	-1.70	-1.55
E_{*O}/ eV	-1.99	-1.87	-1.85
E_{*OOHs}/ eV	1.38	1.42	-
E_{*OOHd}/ eV	1.60	1.70	1.84
E_{*OOHs} - E_{*OH}/ eV	3.19	3.12	-
E_{*OOHd} - E_{*OH}/ eV	3.41	3.40	3.39

The adsorption energy difference E_{*OOH} - E_{*OH} for $NaTaO_3$ is in accord with the universal scaling relationship between HO* and HOO* on metal or metal oxide surface[5, 6], namely E_{*OOH} - $E_{*OH} \approx 3.2$ eV.
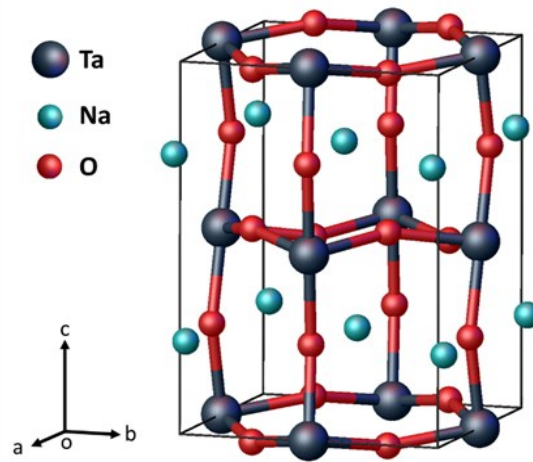
Figure S1. Atomic structure of orthorhombic $NaTaO_3$ unit cell, the lattice constant is a = 5.470 Å, b = 5.545 Å, c =7.801 Å, $\alpha = \beta = \gamma = 90°$. The theoretically calculated and experimentally determined bulk lattice constant (a = 5.494 Å, b = 5.513 Å, c = 7.750 Å, $\alpha = \beta = \gamma = 90°$) are nearly identical. Ta: dark blue spheres, Na: cyan green spheres, O: red spheres.
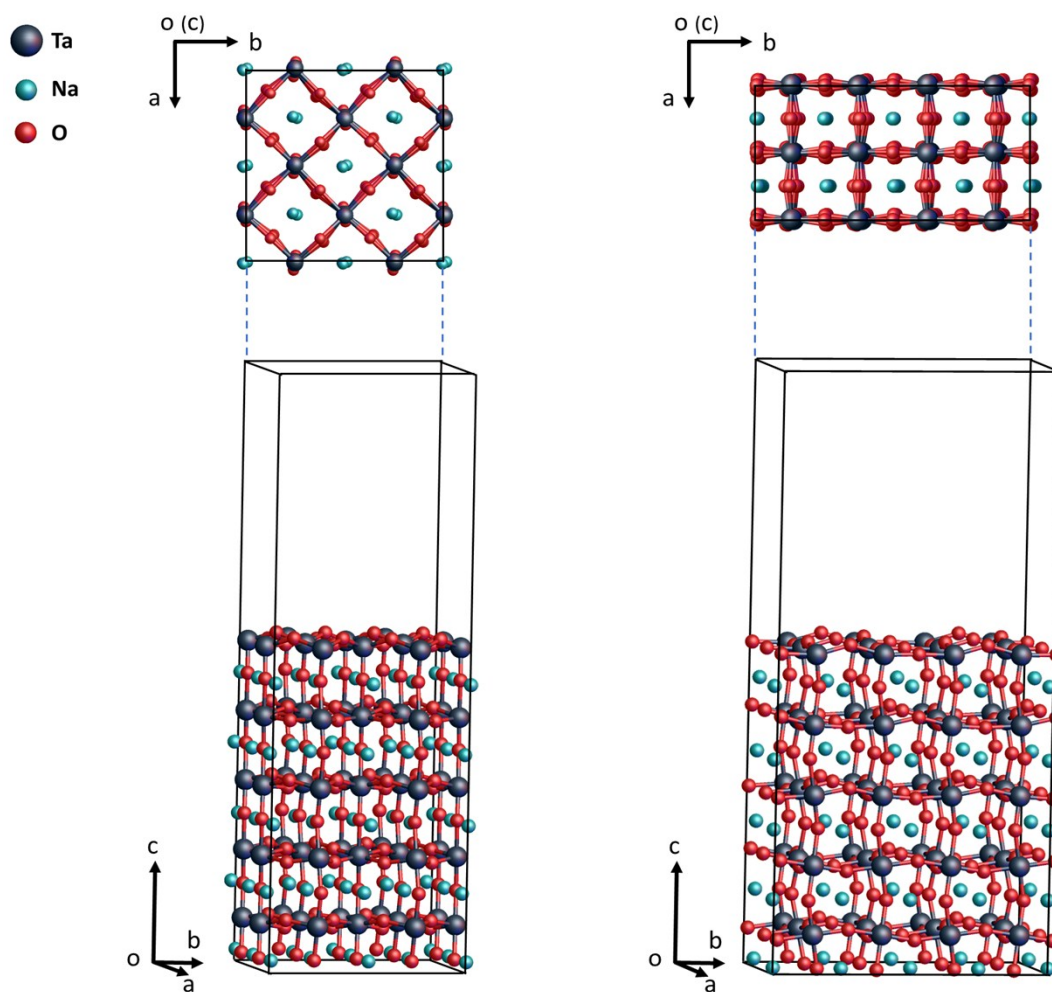
Figure S2. Atomic structure of (A) NaTaO$_3$ (001) slab and (B) NaTaO$_3$ (110) slab with no adsorbate. The lattice constant for NaTaO$_3$ (001) slab is a = 10.939 Å, b = 11.090 Å, c = 33.849 Å, $\alpha = \beta = \gamma = 90°$, the lattice constant for NaTaO$_3$ (110) slab is a = 7.801 Å, b = 15.578 Å, c = 34.002 Å, $\alpha = \beta = \gamma = 90°$. Ta: dark blue spheres, Na: cyan green spheres, O: red spheres.
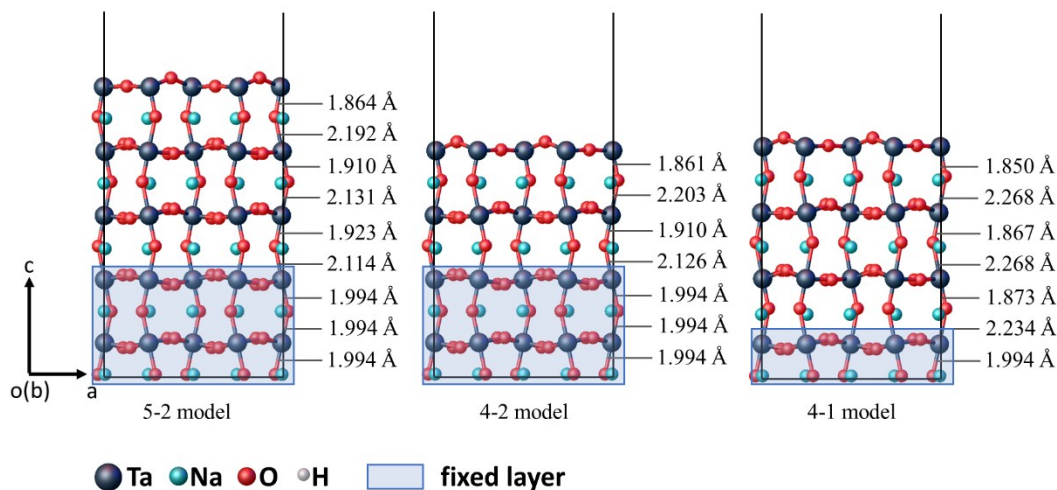
Figure S3. Comparison of different slab model for NaTaO$_3$ (001) surface. The Ta-O bond length between atoms at different layers are shown on the diagram. A 16 Å vacuum was introduced in all these three slabs.

In a recent paper, Ouhbi and Aschauer[7] modeled water oxidation on NaTaO$_3$ and proposed free energy diagram and mechanism that are quantitatively and qualitatively different than ours. They used a slab model of NaTaO$_3$ (001) that included four layers, with the bottom layer frozen during structure optimization. We refer to it as a 4-1 model.

To confirm our findings, we carried out calculations with the 4-1 model, a 4-2 model (four layers - two frozen layers), and with a 5-2 model (five layers - two frozen layers) using the method reported in **Section 3. Computational Method**. It is widely accepted that thicker slabs are 'better' models. Accordingly, we believe that the data arising from the 5-2 model ought to be considered more accurate than those from the 4-1 and 4-2 models. The optimized slab structures are displayed in Figure S3. It is noticeable that the 4-1 model has a structure with pronounced alternating Ta-O and O-Ta distances in the z direction. This behavior carries from the frozen layer up to the

14

surface layer. The alternating behavior in the 4-2 or 5-2 model is much reduced and more consistent with the bulk structure of $NaTaO_3$ with Ta-O distances $\sim$ 1.994 Å. We believe the stronger alternance of Ta-O bonds near the surface is a symptom of the calculated differences in binding energies of the adsorbates.
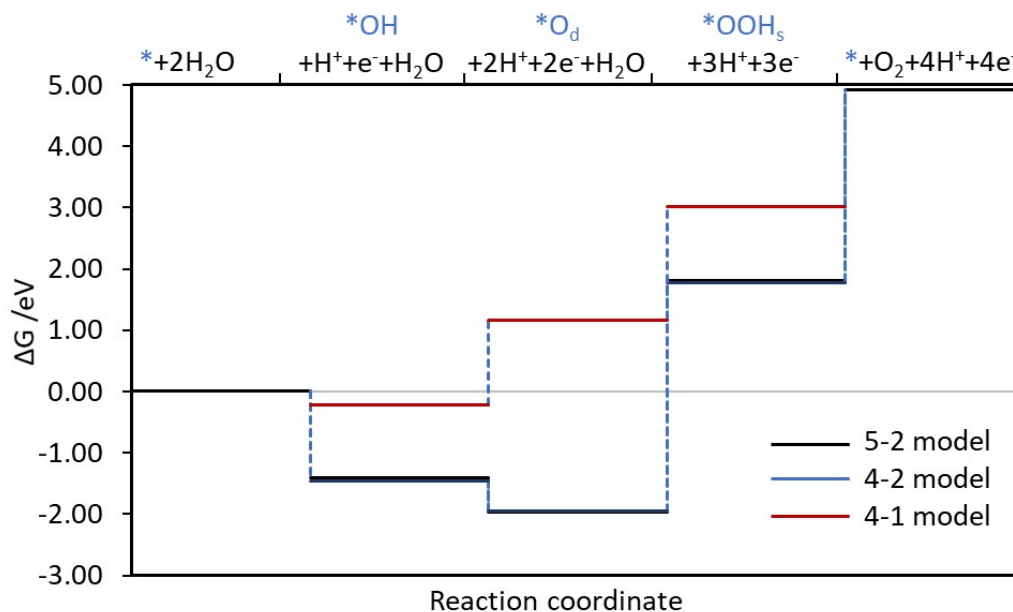
Figure S4. Energy landscapes for water oxidation on $NaTaO_3$ (001) surface at pH = 0. The paths noted by black, blue and red color correspond the 5-2 model, 4-2 model and 4-1 model, respectively. The landscapes for the 5-2 and 4-2 models almost overlap.

The water oxidation energy diagrams based on the intermediate's relative energies (Table S2) is displayed in Figure S4. The water oxidation free energy diagram arising from the 4-1 model is similar to the one from Ouhb and Aschauer[7], suggesting that our VASP/PAW calculations are technically correct. However, the diagram from the 4-1 model is very different from the diagrams of the other two models that almost overlap. The consistency between the 4-2 and the 5-2 model suggest that the models have converged, and we take the 5-2 model as the better model to study the mechanism.
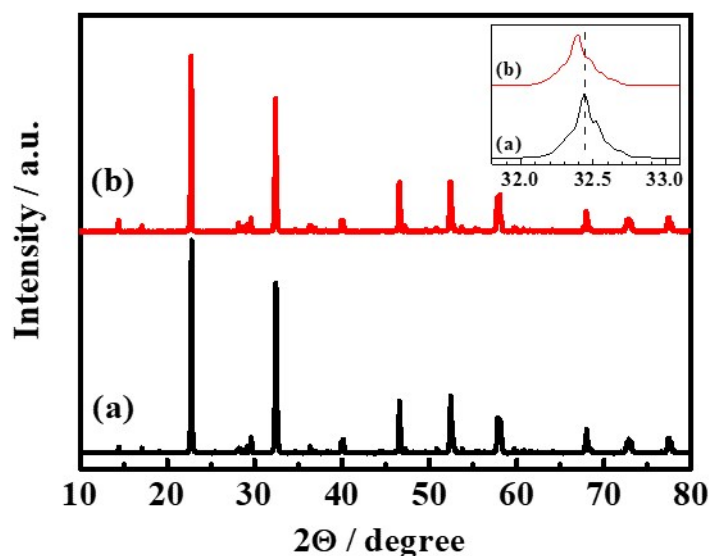
Figure S5. XRD patterns of (a) $NaTaO_3$, and (b) $NaTaO_3$:La (2 mol%).

X-ray diffraction (XRD) measurement was carried out on a Rigaku D/Max-2500/PC powder di□ractometer (Cu Kα radiation) with operating voltage of 40 kV and operating current of 200 mA. The XRD patterns for both $NaTaO_3$ and $NaTaO_3$:La demonstrate that they are in perovskite structure with high crystallinity. The small XRD peaks at 14.5, 17.1, 28.7, 29.2, 29.6, 36.3 degrees are attributed to trace $Na_2Ta_4O_{11}$, the presence of which is unlikely to affect the water oxidation mechanisms. The slightly shift of the XRD patterns as shown in the inset indicates that a part of lanthanum at least was homogeneously doped into the $NaTaO_3$.[2] The shift suggests the substitution of La^{3+} for Na^+ in the bulk.
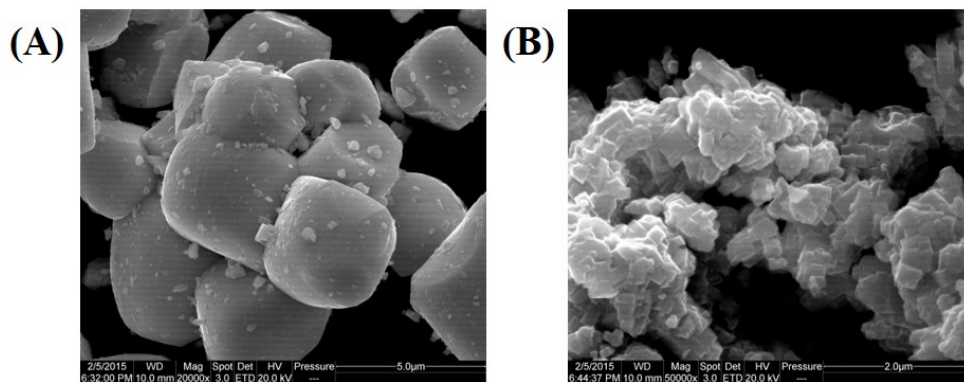
Figure S6. SEM images of (A) NaTaO$_3$, (B) NaTaO$_3$:La (2 mol%).

Surface morphologies of samples were studied by the scanning electron microscope (SEM) on Quanta 200 FEG. The particle sizes of NiO/NaTaO$_3$:La, ~0.3 μm, are remarkably smaller than that of NaTaO$_3$，~2.5 μm. Both the photocatalysts are well-crystallized. The decrease in the particle size with the high crystallinity is beneficial to the photocatalytic reactions, resulting the improved photoactivity of NaTaO$_3$:La.
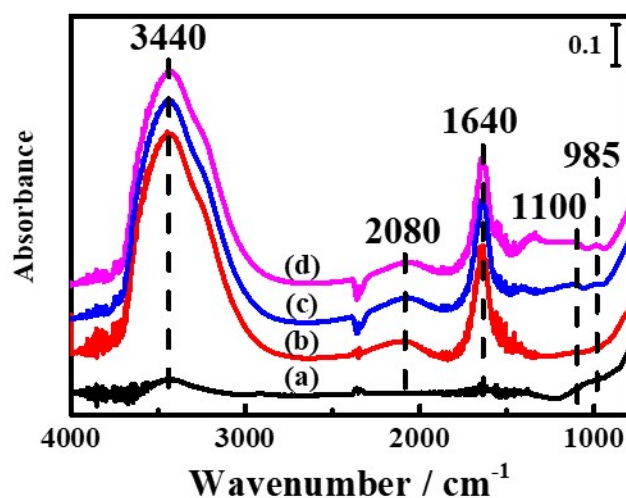
Figure S7. Difference FT-IR spectra of (a) $NaTaO_3$ in air; H_2O adsorbed on (b) $NaTaO_3$, (c) $NaTaO_3$:La (2 mol%) and (d) 0.2 wt% $NiO/NaTaO_3$:La (2 mol%).

Figure S7 shows the difference FT-IR spectra of $NaTaO_3$ samples in air/water vapor. The IR peaks at 3440 and 1640 cm^{-1} are assigned to the OH stretching and the HOH bending resulting from the water adsorption. The IR band centered at 2080 cm^{-1} can be ascribed to the second overtone of the vibrational mode of water. There appear two IR peaks centered at 1100 and 985 cm^{-1}, different from the 1060 and 935 cm^{-1} on UV-irradiated $NaTaO_3$. The IR band at 1100 cm^{-1} is tentatively assigned to the bending mode of the adsorbed OH group as its intensity increases with an increase in water vapor, The IR band at 985 cm^{-1} may be associated with water adsorbed on O vacancy on the basis of saturation observed with an increase in water vapor.

It is possible that the appearance of the 1060 and 935 cm^{-1} peaks results from the desorption of water induced by light irradiation. This possibility is excluded by the control experiments in Figure S8a-c. That is, the 1060 and 935 cm^{-1} peaks were not observed in $NaTaO_3$ samples without NiO cocatalyst under 266 nm irradiation (Figure

S8a-b), in spite of the same effect of water desorption. Moreover, there were no 1060 and 935 cm^{-1} peaks observed either under the 532 nm irradiation (Figure S8c). These results demonstrate that the two peaks in Figure 1 and S7 are induced by different reasons.
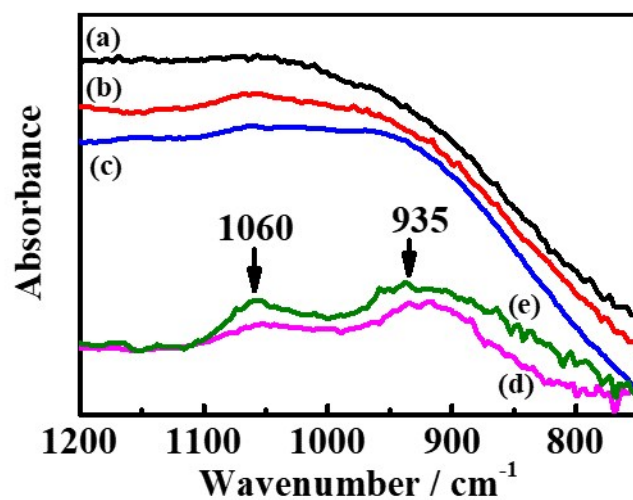
Figure S8. Difference FT-IR spectra of H_2O adsorbed on (a) $NaTaO_3$, (b) $NaTaO_3$:La (2 mol%), (d) 0.2 wt% $NiO/NaTaO_3$, (e) 0.2 wt% $NiO/NaTaO_3$:La (2 mol%) after 266 nm laser (20 Hz,70 mW) irradiation and (c) 0.2 wt% $NiO/NaTaO_3$:La (2 mol%) after 532 nm laser (20 Hz,70 mW) irradiation for ~60 min.
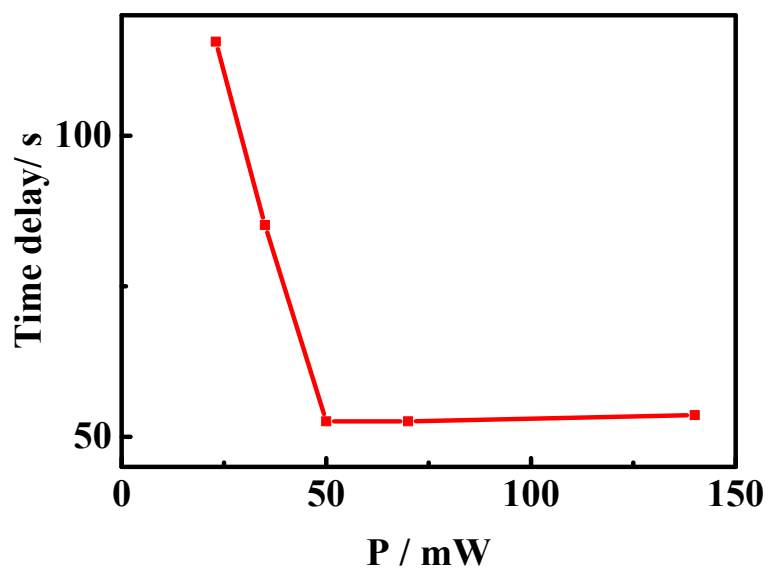
Figure S9. Laser power-dependent time delay from the time to start UV irradiation for the appearance of the band at 935 cm^{-1}. In these experiments, 30 spectra were averaged and the spectra were scanned 5 times.
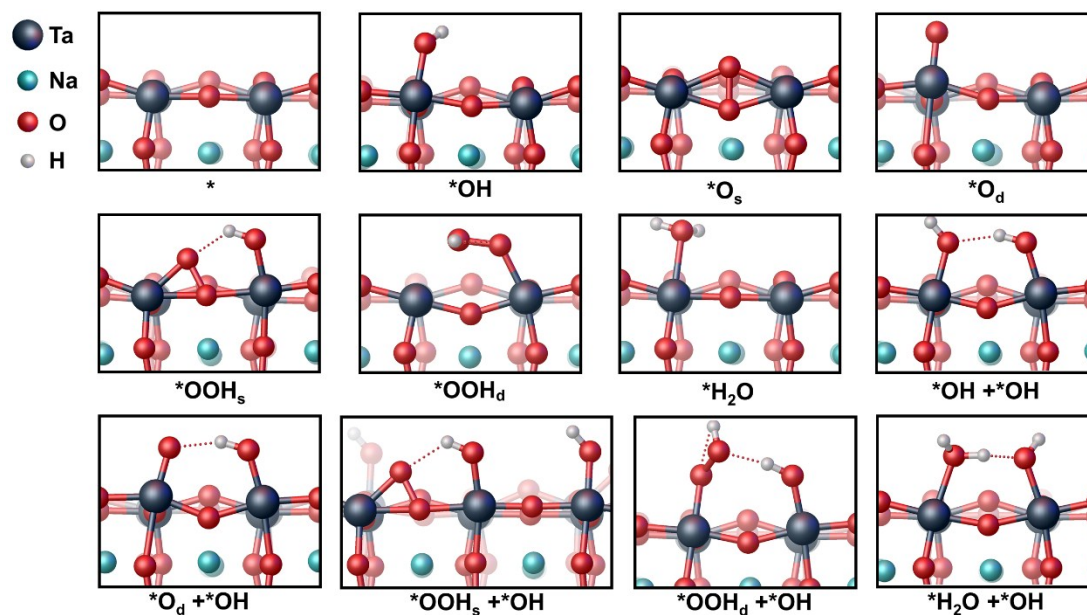
Figure S10. Geometries of possible water oxidation intermediates on NaTaO$_3$ (001) surface. Water oxidation intermediates on (110) surface have very similar structures with (001) surface. Ta: dark blue spheres, Na: cyan green spheres, O: red spheres, H: white spheres.
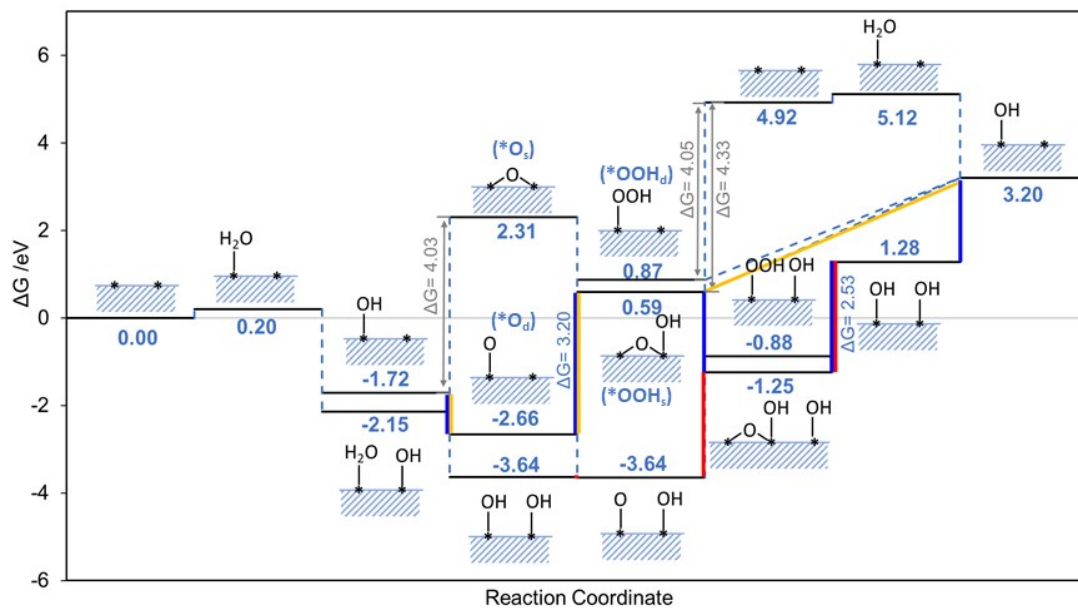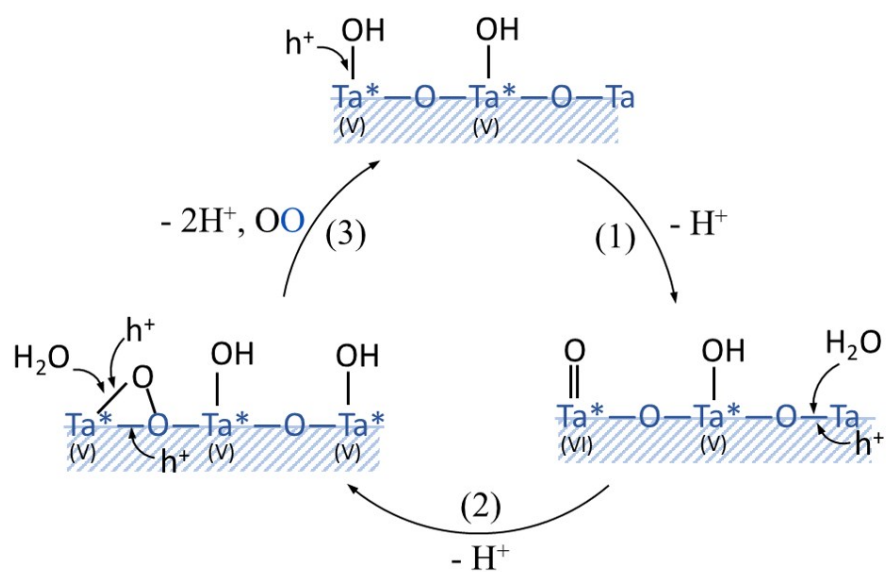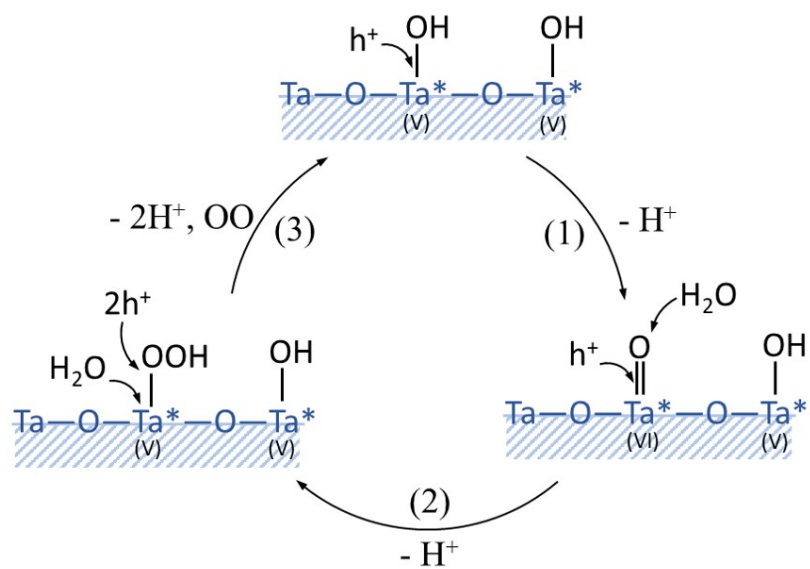
Figure S11. Energy landscapes for water oxidation on (110) surface at pH = 7. The path noted by yellow, red and blue color corresponds the *M1*, *M2* and *M3* mechanism, respectively.
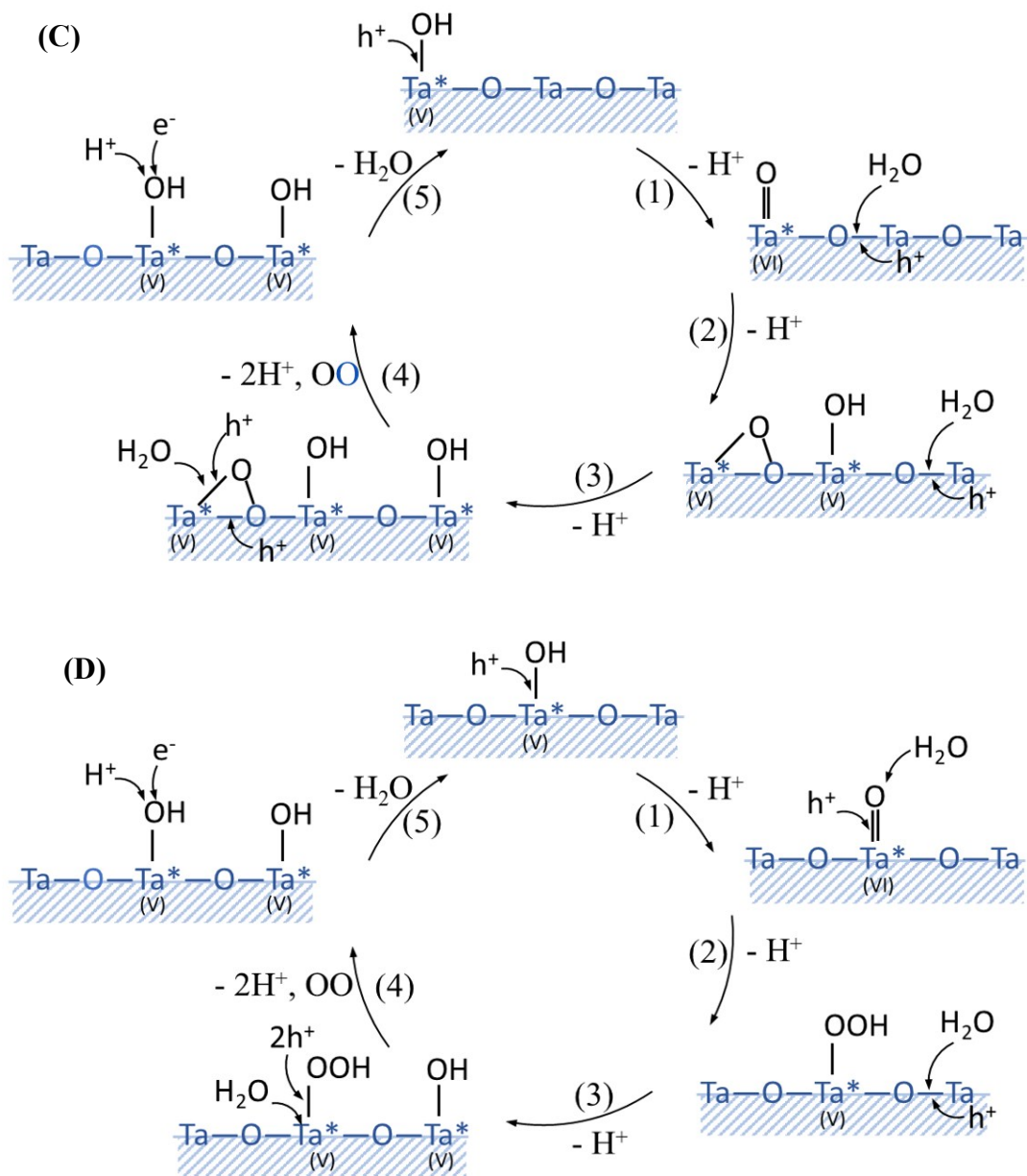
(A)

(B)

Figure S12. Proposed reaction mechanism for photocatalytic water splitting reaction on NaTaO$_3$-based catalysts based on **M2** (A and B) and **M3** (C and D) mechanisms. The evolved O$_2$ is ^{16}O^{18}O from lattice oxygen mechanisms (A, C) or ^{18}O^{18}O from water nucleophilic attack mechanisms (B, D). The lattice oxygens (^{16}O) from NaTa^{16}O$_3$ are marked in blue, while the water oxygens (^{18}O) from H$_2$^{18}O are marked in black.

References

1.   Valdes, A.; Qu, Z. W.; Kroes, G. J.; Rossmeisl, J.; Nørskov, J. K., Oxidation and Photo-Oxidation of Water on TiO_2 Surface. *J. Phys. Chem. C* **2008**, *112*, 9872-9879.

2.   Kato, H.; Asakura, K.; Kudo, A., Highly Efficient Water Splitting into H_2 and O_2 over Lanthanum-Doped $NaTaO_3$ Photocatalysts with High Crystallinity and Surface Nanostructure. *J. Am. Chem. Soc.* **2003**, *125*, 3082-3089.

3.   Dionigi, F.; Vesborg, P. C. K.; Pedersen, T.; Hansen, O.; Dahl, S.; Xiong, A.; Maeda, K.; Domen, K.; Chorkendorff, I., Gas Phase Photocatalytic Water Splitting with $Rh_{2-y}Cr_yO_3$/GaN:ZnO in μ-Reactors. *Energy Environ. Sci.* **2011**, *4*, 2937-2942.

4.   Dionigi, F.; Vesborg, P. C. K.; Pedersen, T.; Hansen, O.; Dahl, S.; Xiong, A.; Maeda, K.; Domen, K.; Chorkendorff, I., Suppression of the Water Splitting Back Reaction on GaN:ZnO Photocatalysts Loaded with Core/Shell Cocatalysts, Investigated Using a μ-Reactor. *J. Catal.* **2012**, *292*, 26-31.

5.   Man, I. C.; Su, H.-Y.; Calle-Vallejo, F.; Hansen, H. A.; Martínez, J. I.; Inoglu, N. G.; Kitchin, J.; Jaramillo, T. F.; Nørskov, J. K.; Rossmeisl, J., Universality in Oxygen Evolution Electrocatalysis on Oxide Surfaces. *ChemCatChem.* **2011**, *3*, 1159-1165.

6.   Rossmeisl, J.; Qu, Z. W.; Zhu, H.; Kroes, G. J.; Nørskov, J. K., Electrolysis of Water on Oxide Surfaces. *J. Electroanal. Chem.* **2007**, *607*, 83-89.

7.   Ouhbi, H.; Aschauer, U., Water Oxidation Catalysis on Reconstructed $NaTaO_3$ (001) Surfaces. *J. Mater. Chem. A* **2019**, *7*, 16770-16776.